Journal of Fluids and Structures (1999) **13,** 499–518
Article No.: jfls. 1999.0214. available online at http:/www.idealibrary.com on IDEAL

EFFECTS OF FREE-END CONDITION ON END-CELL-INDUCED VIBRATION

T. KITAGAWA,

Department of Civil Engineering, Nihon University, 1-8 Kanda-Surugadai, Chiyoda-ku Tokyo 101-8308, Japan

AND

Y. FUJINO AND K. KIMURA

Department of Civil Engineering, The University of Tokyo, 7-3-1 Hongo, Bunkyo-ku, Tokyo 113-8656, Japan

(Received 2 March 1998 and in revised form 5 November 1998)

Wind tunnel experiments were conducted to investigate the characteristics of the transverse-wind vibration of a pivoted circular cylinder. It is confirmed that a vibration, which is similar to the vortex-induced vibration, occurs at a wind speed higher than the threshold wind speed for the vortex-induced vibration. Special attention is paid to the cause of that vibration. In this study, that vibration is called as "end-cell-induced vibration (ECIV)", and the mechanism of ECIV is investigated. The measurement of the wind velocity fluctuation behind the model at various heights indicates that vortices whose frequency is much lower than the Karman vortex shedding frequency are generated around the free end of the model. This vortex is called "tip-associated vortex" in this study. ECIV occurred at the wind speed where the frequency of these vortices coincides with the natural frequency of the model. Therefore, ECIV is thought to be caused by tip-associated vortex shedding. Furthermore, based on the conjecture which the three-dimensional flow around the free-end affects the generation of the tip-associated vortices, a thin circular disk is attached to the model top and its diameter is varied. The effects of the circular disk on ECIV and on the generation of the tip-associated vortices are studied experimentally.

1. INTRODUCTION

IT HAS BEEN WELL KNOWN that the vortex-induced vibration of a circular cylinder occurs around the particular wind speed where the vortex-shedding frequency coincides with one of the natural frequencies of the structure. Although many studies have been made on vortex-induced vibration (VIV), most of them consider the phenomenon only around the above-mentioned wind speed.

On the other hand, some experimental studies using cantilevered circular cylinders indicate that not only VIV but also a vibration similar to vortex-induced vibration occurs at a wind speed a few times higher than the threshold wind speed of VIV. That vibration will be called the "end-cell-induced vibration (ECIV)" in this study.

Wootton (1969) carried out wind tunnel experiments using circular stack models and measured the transverse-wind response, which indicates the occurrence of ECIV at a wind speed twice as high as the wind speed where VIV occurred. He inferred that the cause of ECIV is associated with the tip of the model, but no evidence was presented in his paper.

0889–9746/99/040499 + 20 $30.00

Similarly, Kawai (1994) conducted wind tunnel experiments using circular cylinder rocking models and obtained the response of ECIV at a wind speed 2·5 times higher than the threshold wind speed of VIV. In the power spectrum of the transverse-to-wind response, a peak due to the aerodynamic force whose frequency was lower than the Karman vortex shedding frequency appeared.

Kitagawa *et al.* (1998), in order to elucidate the mechanism of ECIV, conducted a wind tunnel experiment using a circular cylinder rocking model. The transverse-wind response and the wind velocity fluctuations behind the model at various heights were measured. It was shown that the response peak due to ECIV can be observed under a uniform flow. The power spectra of the wind velocity fluctuations behind the model indicated that a fluctuation different from that due to the Karman vortex was generated around the free-end. This fluctuation is referred to as being due to "tip-associated vortex shedding", and its frequency was found to be lower than the Karman vortex shedding frequency. Since ECIV occurred at a wind speed where the frequency of the tip-associated vortex shedding coincided with the natural frequency, it was thought that ECIV was induced by the tip-associated vortices.

In this study, to further confirm that the tip-associated vortices are generated by three-dimensional flow around the model top, the effects of the free-end condition on the generation of the tip-associated vortices as well as the occurrence of ECIV are studied. Firstly, an experiment using a pivoted circular cylinder is carried out to confirm the occurrence of ECIV, and the results are compared with those obtained by Kitagawa *et al.* (1998). Secondly, a thin light circular disk is attached to the top of the model. Varying the diameter of the disk, the effects on the generation of the tip-associated vortices and the model response due to ECIV are discussed.

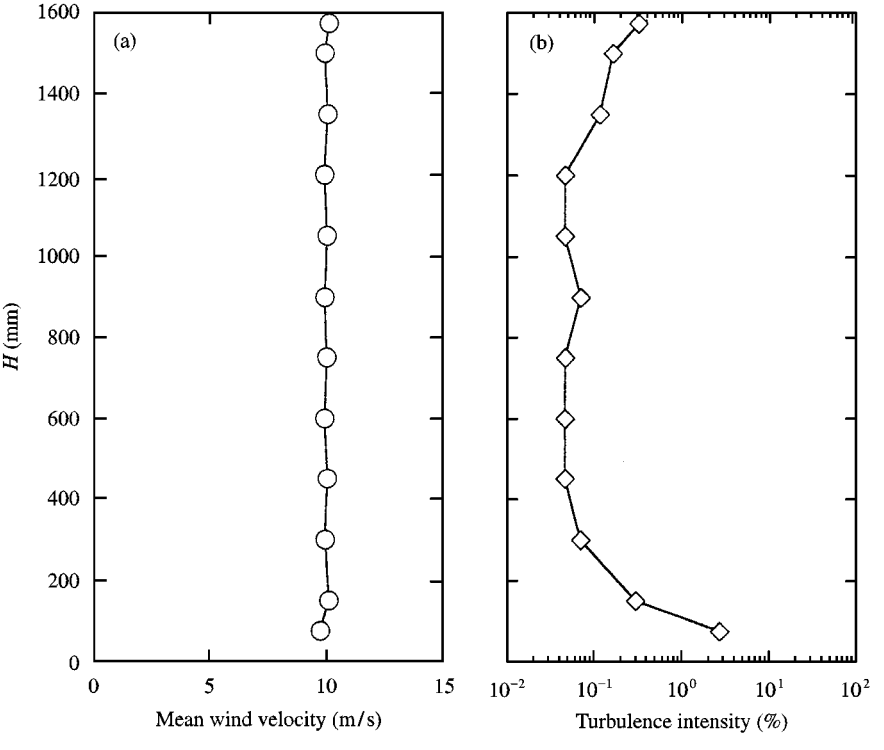

Figure 1. Profiles of the approaching flow at $V = 10$ m/s. (a) Mean wind velocity; (b) turbulence intensity.

2. EXPERIMENT

The experiments were conducted at the closed circuit wind tunnel in the Department of Civil Engineering, the University of Tokyo. The test-section of the wind tunnel is 1·8 m high and 1·5 m wide. The profiles of the mean velocity and the turbulent intensity of approaching flow are shown in Figure 1(a,b). These profiles were based on the data measured at a mean wind speed V of 10 m/s. Although the boundary layer generated by the friction of the wind tunnel floor was seen at $H < 100$ mm (H being the height from the floor of the test-section), the flow was almost uniform.

As shown in Figure 2, a rigid circular cylinder cantilevered by a steel leaf-spring was used. The model allows single-degree-of-freedom rocking motion only in the transverse-to-wind direction. The height of the cylinder itself, H_c, was 1250 mm, and the diameter, D_c, was 50 mm. The cylinder was mainly made of cypress and balsa. Also, to achieve adequate

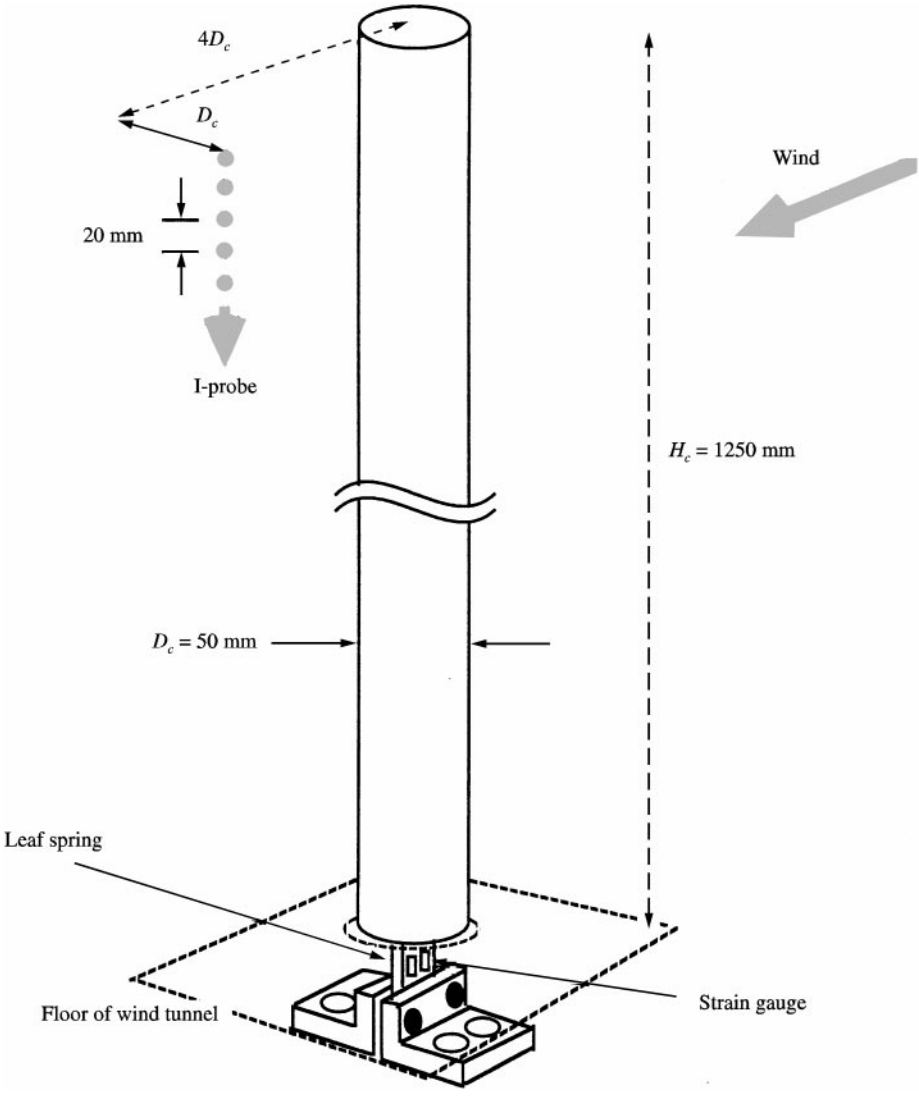

Figure 2. Experimental model and measurement set-up.

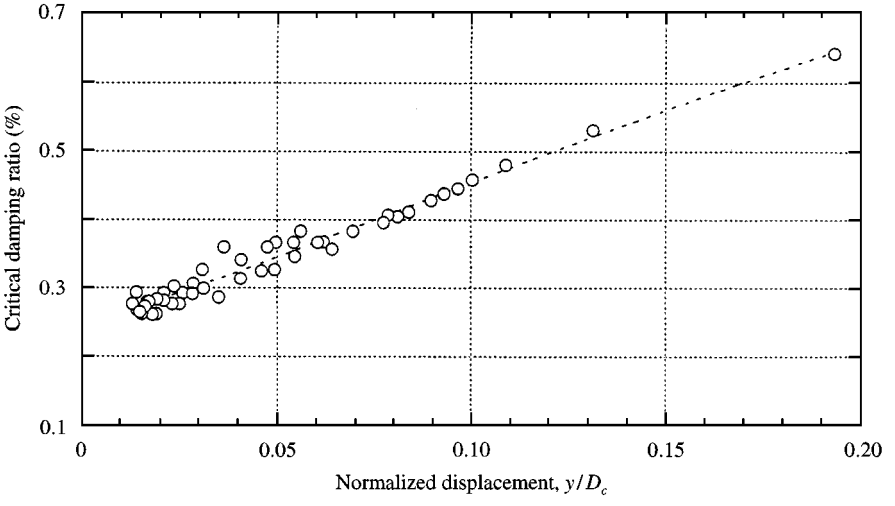

Figure 3. Relationship between the critical damping ratio of the model and normalized displacement at the model top, y/D_c.

rigidity with a light mass, a carbon rectangular tube was installed inside. Total mass of the cylinder part was 760 g. The strain of the leaf-spring was measured by strain gauges and was translated into the transverse-to-wind displacement at the model top, y. The natural frequency f_n was 6·4 Hz and the structural damping ratio ξ, which was investigated by a series of decay tests starting at different amplitudes, has a slight amplitude dependency, as shown in Figure 3. The Scruton number $2\pi\xi J/\rho D_c^2 H_c^3$, where J is moment of inertia and ρ is air density, was approximately 0·74 for a measured ξ of 0·003. An I-type hot-wire probe was used to measure the fluctuating wind velocity behind the model. The position of the probe was $4D_c$ downstream, and D_c aside from the center of the model. The vertical location of the probe was varied in the range of $0 < H \leqslant 1250$ mm with a 20 mm pitch. The measurements were done at Reynolds number (= Re) $< 3{\cdot}3 \times 10^4$.

The sampling of data of the model response and the wind velocity fluctuations was carried out at 500 Hz. The data of the model response was low-pass filtered at 71 Hz and that of wind velocity fluctuation was done at 224 Hz.

3. RESULTS

3.1. Model Response Amplitude

The relationship between the reduced velocity V/f_nD_c and the normalized (r.m.s.) displacement of the cylinder y/D_c is shown in Figure 4. The vortex-induced vibration (VIV) started at $V/f_nD_c = 5{\cdot}0$ and has a peak value at $V/f_nD_c = 6$. Another peak is seen at $V/f_nD_c = 14$, and this peak corresponds to ECIV, which is mainly discussed in this study.

Additionally, the result obtained in a previous experiment by Kitagawa *et al.* (1998) is plotted with a dotted line. The size of that model was 1/2·5 of the present model, while the aspect ratio was the same. It was difficult to compare the response amplitude qualitatively, because the damping ratio of the model in the present experiment was not constant with transverse-to-wind displacement, as shown in Figure 3. However, the amplitude of VIV was nearly the same for those two cases. On the other hand, the amplitude of ECIV in the present case was larger than that obtained by Kitagawa *et al.* while the threshold wind speed of ECIV was somewhat lower. Although the reason why the threshold wind speed is

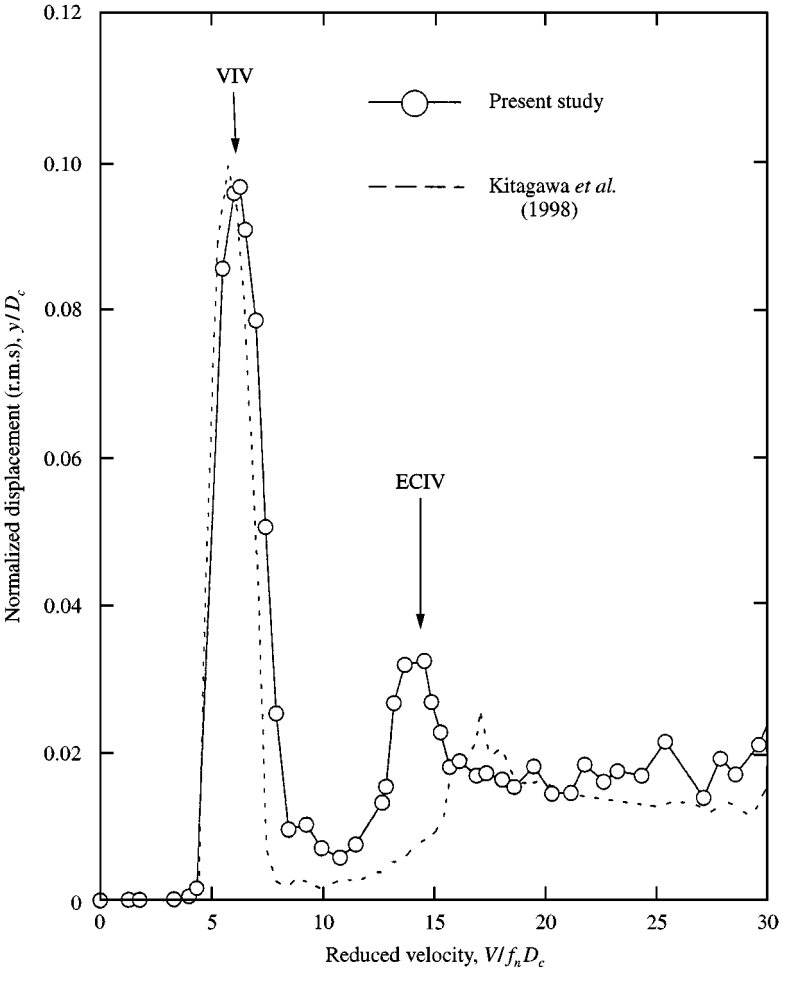

Figure 4. Transverse-to-wind (r.m.s.) displacement of the model, y/D_c, versus reduced velocity, V/f_nD_c, and comparison with the result by Kitagawa *et al.* (1998). The size of the model used by Kitagawa *et al.* was 1/2·5 times as large as that of the present study, while the aspect ratio was the same.

shifted is unknown, the difference of the profiles of the approaching flow is thought to be one of the causes.

The time histories at $V/f_nD_c = 6$, 10 and 14 are, respectively, shown in Figure 5(a), (b) and (c). ECIV at $V/f_nD_c = 14$ [Figure 5(c)] had an unsteady amplitude, while the amplitude of VIV at $V/f_nD_c = 6$ [Figure 5(a)] was nearly constant. On the other hand, the amplitude at $V/f_nD_c = 10$ [Figure 5(b)], where the r.m.s. value was very small as shown in Figure 4, had some irregularity. It is thought that this vibration mainly includes the buffeting response due to weak turbulence of the approaching flow.

3.2. Characteristics of Vortex-Shedding Frequency

In the previous section, the occurrence of ECIV was confirmed. In this section, the cause of ECIV is investigated through the power spectra of wind velocity fluctuations behind the model and the model response.

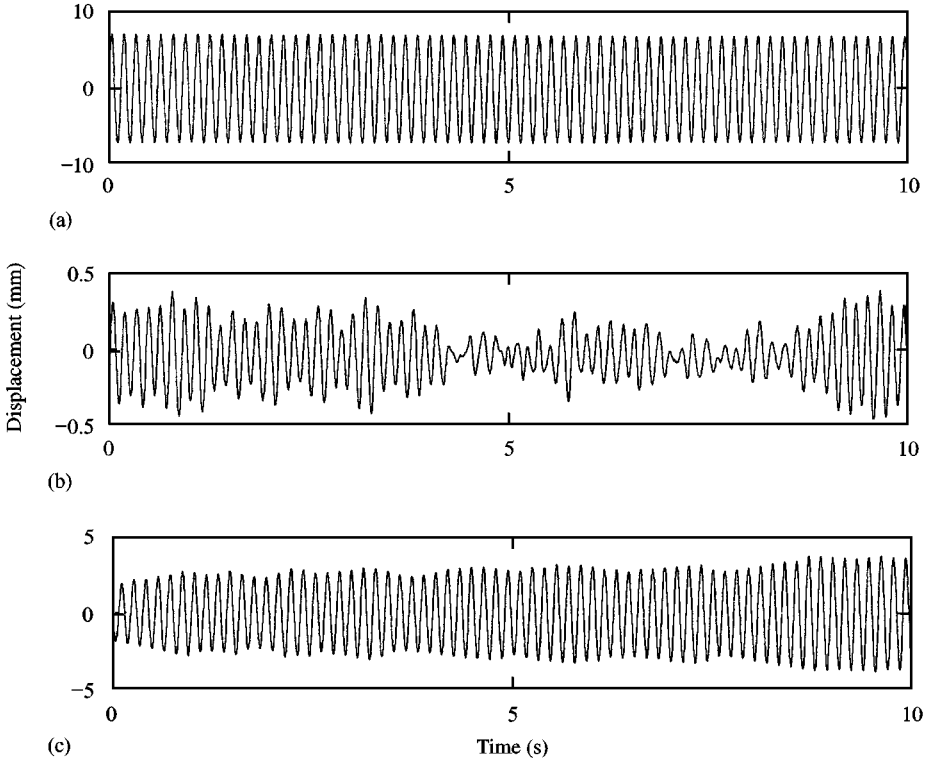

Figure 5. Time histories of the transverse-to-wind response. (a) Vortex-induced vibration (VIV) at $V/f_nD_c = 6$; (b) response at $V/f_nD_c = 10$; (c) end-cell-induced vibration (ECIV) at $V/f_nD_c = 14$.

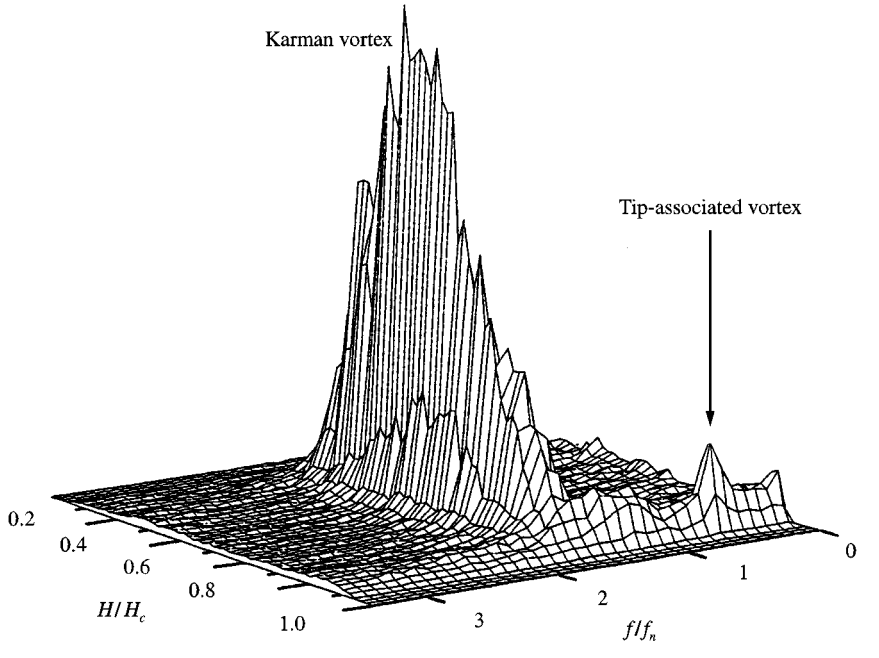

Figure 6. Power spectra of the wind velocity fluctuations behind the model at $V/f_nD_c = 10$ versus normalized frequency f/f_n and normalized height H/H_c.

In Figure 6, the power spectra of wind velocity fluctuations behind the model at $V/f_n\ D_c = 10$ (Re $\simeq 1{\cdot}1 \times 10^4$), where the response amplitude was very small as shown in Figure 4, is shown as a three-dimensional graph with axes of normalized frequency, f/f_n, and normalized height, H/H_c. This graph was obtained by spectral analysis applied to the series of wind velocity fluctuations measured as shown in Figure 2. $H/H_c = 1{\cdot}0$ corresponds to the height at the top of the model, and $H/H_c = 0{\cdot}0$ to the height at the bottom. The large peak due to the Karman vortex shedding was found at $0{\cdot}2 < H/H_c < 0{\cdot}8$ and around $f/f_n = 1{\cdot}88$ (St $\simeq 0{\cdot}2$, where St is the Strouhal number). The height where the most intensive generation of the Karman vortices was observed was approximately $H/H_c = 0{\cdot}5$. At $H/H_c < 0{\cdot}1$, the generation of the Karman vortices was weak because of the turbulence due to the tunnel floor. A small peak was found at $f/f_n = 0{\cdot}68$ (St $\simeq 0{\cdot}07$) and $0{\cdot}85 < H/H_c < 0{\cdot}92$, and this peak is due to the tip-associated vortices.

Figure 7 shows the power spectrum of the transverse displacement at the model top at $V/f_nD_c = 10$. Remarkably, the peak at $f/f_n = 1$ was found, which is probably due to the buffeting response shown in Figure 5(b). The peak due to the aerodynamic force by the Karman vortex shedding was found at $f/f_n = 1{\cdot}88$. Furthermore, effects of the fluctuation of the tip-associated vortices observed in Figure 6 appeared as a peak of $f/f_n = 0{\cdot}68$. Khalak & Williamson (1996) measured the lift force of a circular cylinder with free-end at Re = 10 600, and showed that a peak due to Karman vortex shedding, as well as a peak due to a vortex whose frequency was approximately 1/3 of the Karman vortex-shedding frequency appeared in the power spectrum of the lift force. They mentioned that these two peaks were caused by cellular shedding. The tip-associated vortex in the present study possibly corresponds to one of the cells.

The span-wise distribution of vortex-shedding frequencies at several wind speeds is illustrated in Figure 8, which was obtained by the power spectra of the wind velocity

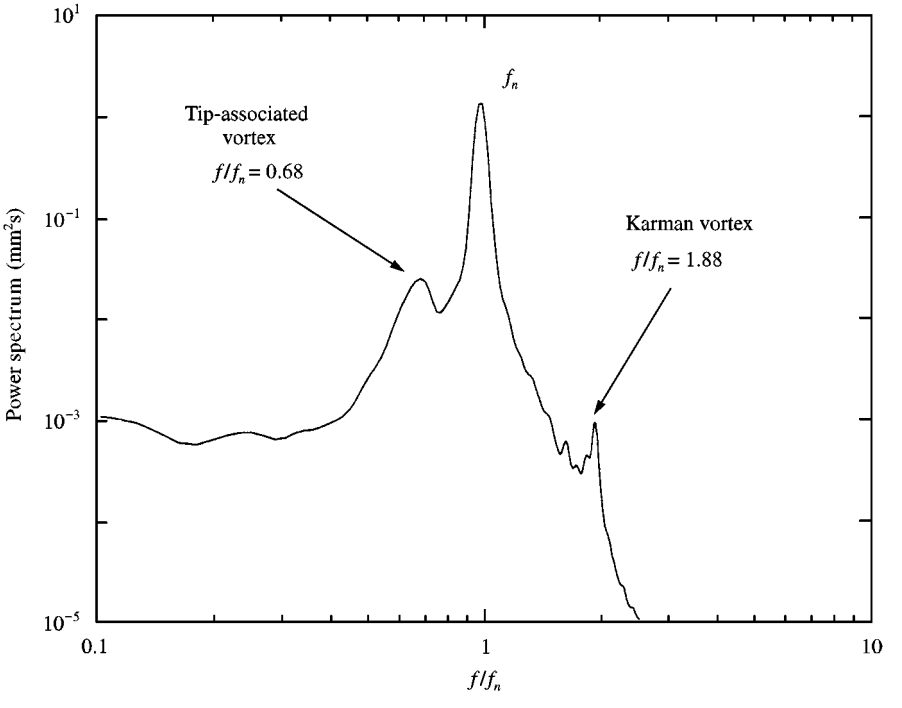

Figure 7. Power spectrum of the transverse-to-wind response at $V/f_nD_c = 10$.

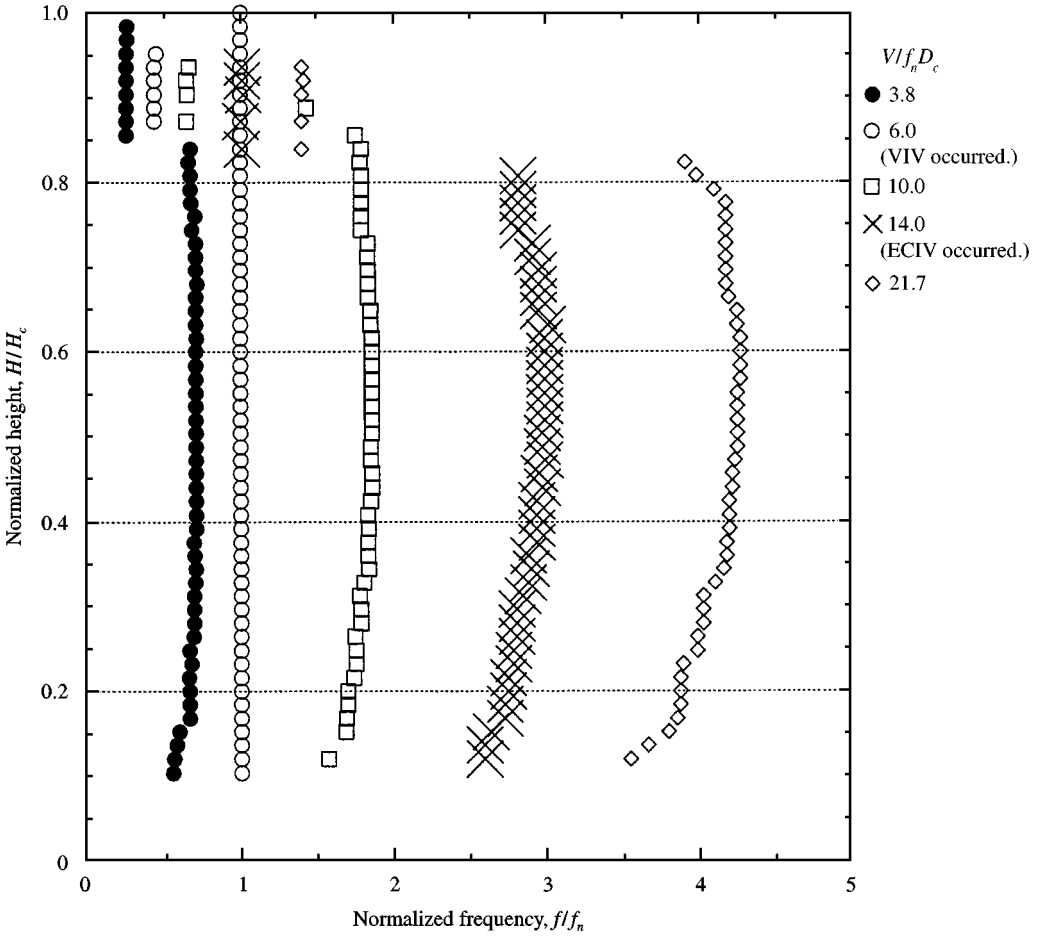

Figure 8. Span-wise distribution of vortex shedding frequencies for various V/f_nD_c: ●, $V/f_nD_c = 3{\cdot}8$; ○, $V/f_nD_c = 6{\cdot}0$ (VIV occurred); □, $V/f_nD_c = 10{\cdot}0$; *x*, $V/f_nD_c = 14{\cdot}0$ (ECIV occurred); ◇, $V/f_nD = 21{\cdot}7$.

fluctuation behind the model. At $V/f_nD_c = 6$ where VIV occurred, the vortex shedding frequency of $f/f_n = 1{\cdot}0$ was seen over the whole height. Also, the tip-associated vortex shedding which had a frequency distinctly lower than the Karman vortex-shedding frequency was observed around the model top. At other wind speeds, the frequency of the Karman vortex shedding gradually varied along the span. Around the model top, tip-associated vortices were generated while the Karman vortex shedding was not observed. Okamoto & Yagita (1973) and Kawamura *et al.* (1984) did not observe vortex shedding around the free end, but observed stationary longitudinal trailing vortices. However, this type of vortex shedding, existing around the free end, has been reported in several other studies, e.g. by Farivar (1981), Ayoub & Karamcheti (1982), and Fox & Apelt (1993). In Figure 8, at $V/f_nD_c = 14$ where ECIV occurred, the frequency coincided with the natural frequency. Then, it is considered that ECIV is caused by the tip-associated vortex shedding. Additionally, Kitagawa *et al.* (1998) investigated the time history of the wind velocity fluctuations around the model top by wavelet analysis and clarified that the nonsteady amplitude of ECIV, as shown in Figure 5(c), was due to the intermittent generation of the tip-associated vortices.

3.3. Relationship Between Vortex-Shedding Frequency and Response

The lower graph of Figure 9 is the relationship between the Karman vortex-shedding frequency at $H/H_c = 0{\cdot}54$ and the wind speed. Also, the model response is depicted with a dotted line. The Karman vortex shedding frequency was proportional to the wind speed,

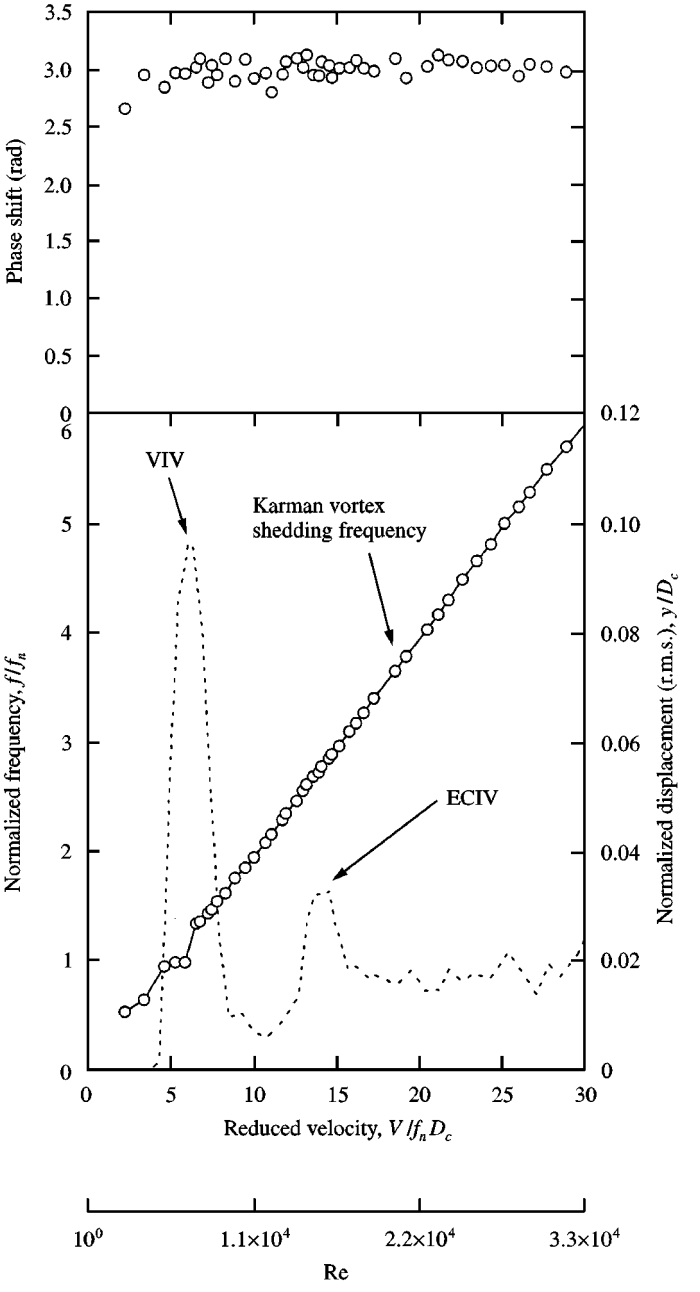

Figure 9. Lower graph: relationship between the Karman vortex-shedding frequency at $H/H_c = 0{\cdot}54$ and the model response. Upper graph: phase shift of Karman vortex shedding, at $H/H_c = 0{\cdot}54$, measured as shown in Figure 10.

and VIV occurred around $V/f_nD_c = 6$, where the frequency coincided with f_n. The lock-in phenomenon was also observed in VIV.

In order to investigate the phase shift of the vortex street, two I-type probes were symmetrically situated downstream of the model as shown in Figure 10, and the wind velocity fluctuations on both sides were simultaneously measured. The upper graph of Figure 9 is the phase shift of the Karman vortex street at $H/H_c = 0{\cdot}54$. The phase shift was almost π (radians) throughout the measured wind speed, which means that staggered vortices of opposite sign are formed and a periodic lift force can be produced.

On the other hand, the lower graph of Figure 11 shows the relationship between the frequency of the tip-associated vortices at $H/H_c = 0{\cdot}92$ and the model response. The frequency of the tip-associated vortices was nearly proportional to the wind speed, although the frequency was much lower than the Karman vortex shedding frequency shown in the lower graph of Figure 9. ECIV occurred at a wind speed where the frequency of the tip-associated vortices coincided with f_n. Comparing with the upper graph of Figure 9, the phase shift of the tip-associated vortices, shown in the upper graph of Figure 11, took various values, although it seems to be close to π around $V/f_nD_c = 14$ where the ECIV occurred. This means that the tip-associated vortices are not alternately generated. Additionally, the lock-in phenomenon of the tip-associated vortices was not clearly observed in the lower graph of Figure 11.

3.4. End-Plate Effects

In this study, as a method to control the flow over the model top and to investigate effects of the free-end condition on the generation of the tip-associated vortices and the occurrence of ECIV, a circular thin disk is placed on the model top as an end-plate.

As shown in Figure 12, the thickness of the circular disk was 0·7 mm and the diameter D_{cd} is varied. The characteristics of the critical damping ratio and the natural frequency of the model did not change, since the weight of those disks was very light (the mass of the disk of $D_{cd} = 55$ mm was only 2·2 g).

3.4.1. *Model response amplitude*

The relationship between V/f_nD_c and y/D_c (r.m.s.) with different D_{cd} configurations is shown in Figure 13. The amplitude of VIV is not influenced by the size of D_{cd}. However, the

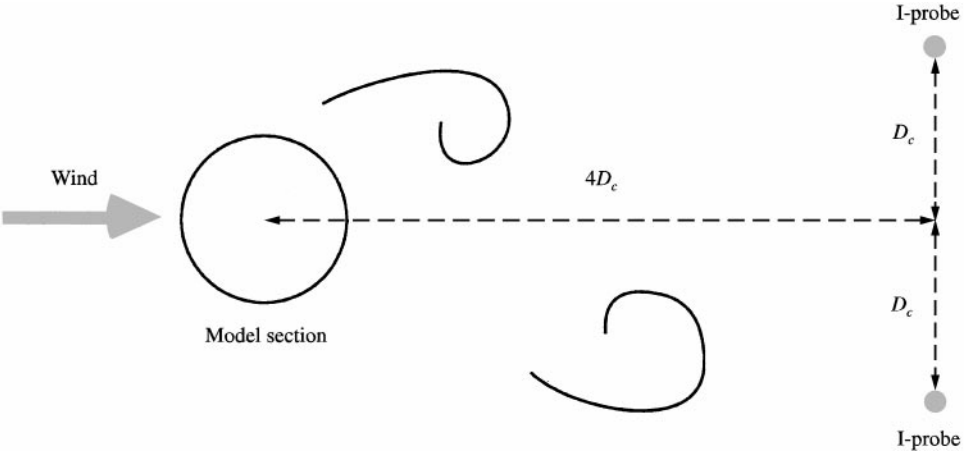

Figure 10. Location of two I-probes to measure the phase shift of vortex sheddings from both sides of the model. The heights of these probes are the same.

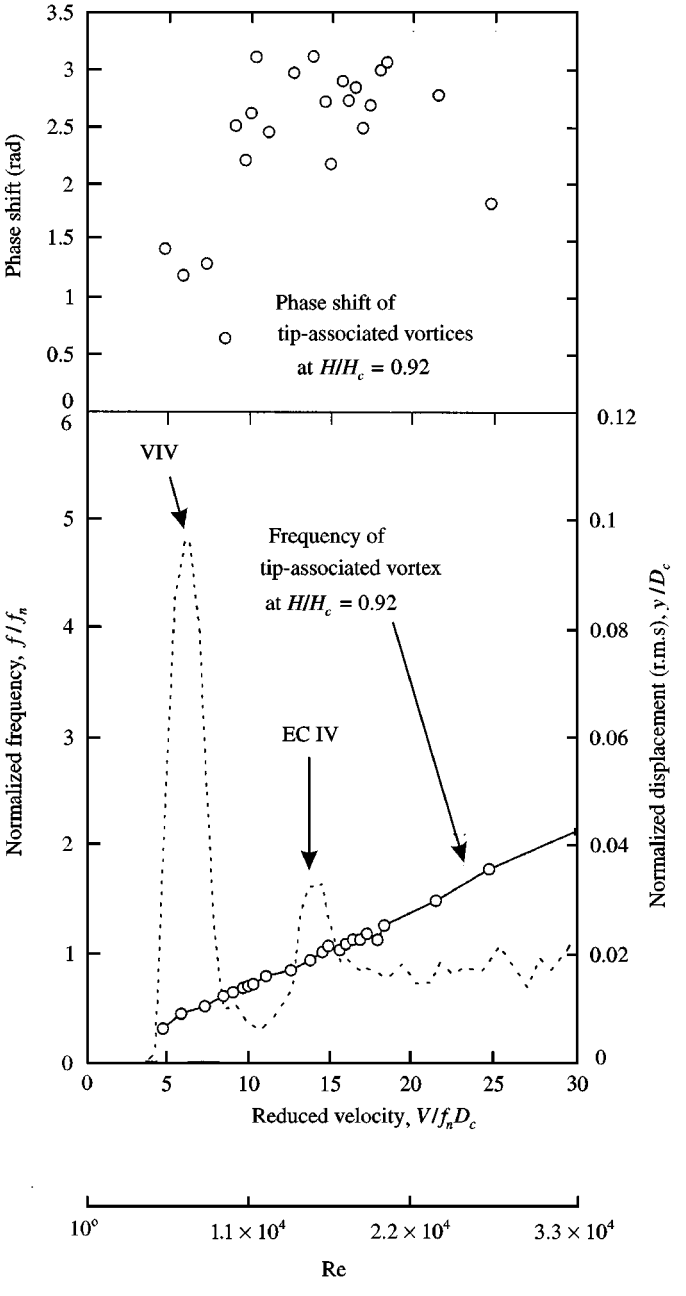

Figure 11. Lower graph: relationship between frequency of the tip-associated vortex shedding at $H/H_c = 0{\cdot}92$ and the model response. Upper graph: phase shift of the tip-associated vortices which was measured as shown in Figure 10.

amplitude of ECIV was significantly reduced by the D_{cd} increase, and the response peak of ECIV was somewhat shifted to ward the low wind-speed region with increasing D_{cd}. Specifically, when D_{cd} was 1·6 times larger than D_c, ECIV almost disappeared. This reason can be explained as follows: the two-dimensionality of the flow around the free-end is enhanced by placing the disk, weakening the generation of the tip-associated vortices, and their frequency becomes high. A detailed discussion will be made in the next section.

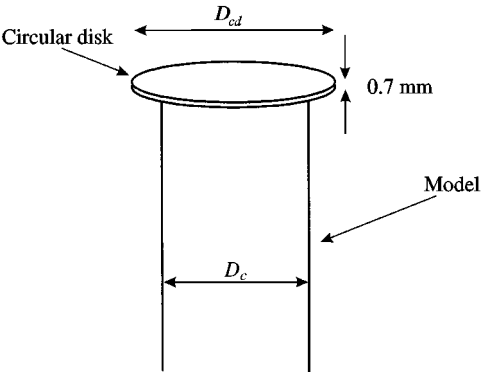

Figure 12. Circular disk placed on the model top.

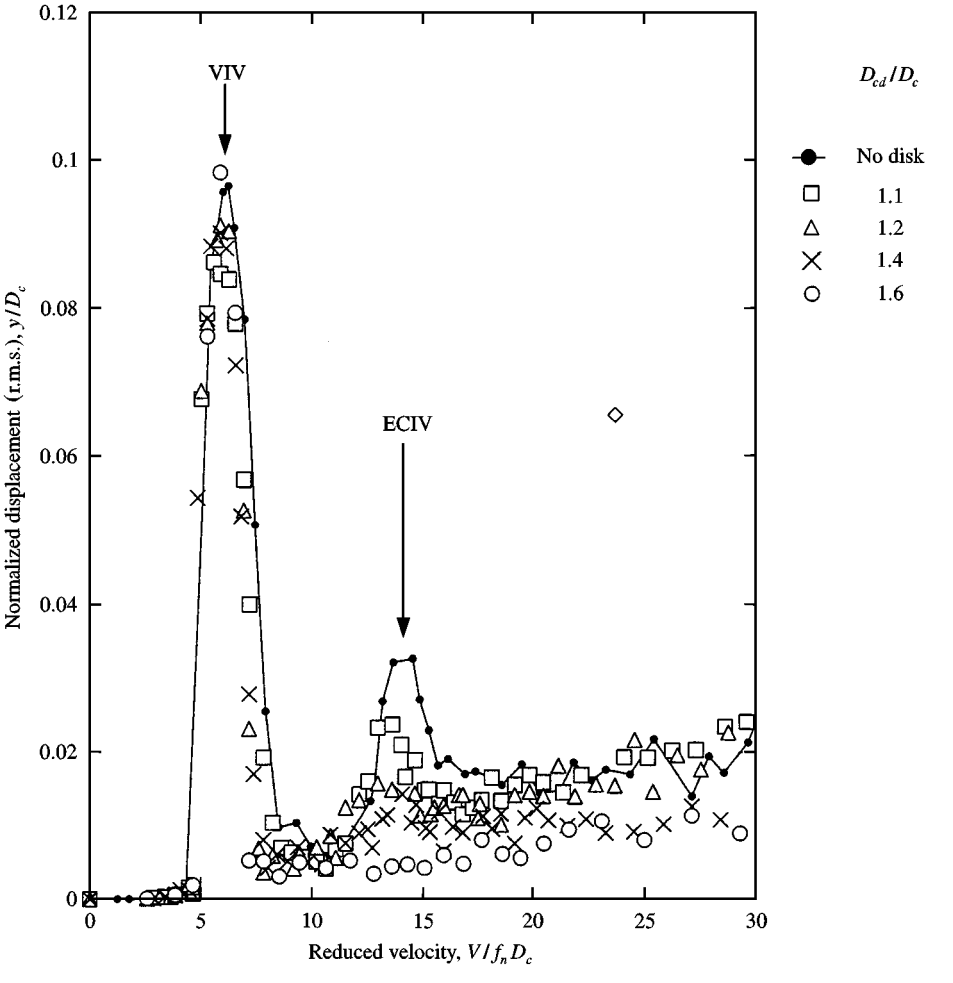

Figure 13. Relationship between D_{cd} and transverse-to-wind response of the model.

Additionally, in Figure 13, we can observe that there is the response amplitude, which was seen at $V/f_nD_c > 10$, and which became large with wind speed increase. This response component is thought to be the self-buffeting caused by turbulence in the wake around the free end, since that response was reduced with the increase in D_{cd}, in spite of using the same approaching flow for all cases.

3.4.2. *Characteristics of vortex-shedding frequency around free end*

In the previous section, it was shown that the response amplitude of ECIV decreased with the increase of D_{cd}. In this section, in order to clarify its mechanism, the relationship between the frequency of the tip-associated vortices and D_{cd} is investigated.

Figure 14(a) shows the power spectrum of the wind velocity fluctuation behind the model without the disk at $H/H_c = 0{\cdot}92$ and $V/f_nD_c = 10$. For comparison, the power spectrum of the Karman vortex shedding at $H/H_c = 0{\cdot}54$ is also shown as a dotted line. At $H/H_c = 0{\cdot}92$, the peak due to the tip-associated vortices was observed at $f/f_n = 0{\cdot}68$. Also, a few tiny peaks were seen in the range of $1 < f/f_n < 2$. In this study, we refer to the vortices causing these tiny peaks as "low-frequency Karman vortices" and they are disucussed in the next paragraph. In the case where the circular disk of $D_{cd}/D_c = 1{\cdot}2$ was placed on the model top [Figure 14(b)], the strength of the tip-associated vortices was decreased. Furthermore, in the case where the disk of $D_{cd}/D_c = 1{\cdot}6$ was placed [Figure 14(c)], the tip-associated vortices almost vanished. Therefore, the reason why the amplitude of ECIV was reduced with increasing D_{cd}/D_c (Figure 13) can be explained by the strength of the tip-associated vortices becoming gradually lower with increasing D_{cd}/D_c. Some studies reported subharmonic oscillations which, similarly to ECIV, occurred at a flow a few times higher than that for VIV occurrence. However, the above-mentioned end-plate effects explain that ECIV does not correspond to those vibrations. Using two-dimensional forced oscillation of a circular cylinder with $y/D_c = 0{\cdot}13$, Ongoren & Rockwell (1988) investigated vortex synchronization. They varied the frequency of forced oscillation and observed the synchronization modes of the vortices via flow visualization. Subharmonic synchronization was observed around $f_e/f_v = 1/2$ (where f_e is the frequency of oscillation, and f_v the frequency of the Karman vortex shedding). There is a possibility that this type subharmonic mode can induce a vibration like ECIV. Moreover, Durgin *et al.* (1980) observed a transverse-wind response peak around $V/f_nD_c = 15$ ($f_n/f_v \simeq 1/3$, which was similar to ECIV in the present study, in a wind tunnel experiment using a two-dimensional circular cylinder. They called this vibration "the lower mode response", and explained that this vibration was a subharmonic response due to the Karman vortex shedding. Now, suppose ECIV is induced by subharmonic synchronization related to Karman vortex shedding. Then, it would be expected that the amplitude of ECIV would hardly be reduced by the disks attached on the top. On the contrary, in the present study it was clearly shown that the amplitude of ECIV decreased in accordance with the tip-associated vortex being weakened by attaching the disks. Thus, it may be concluded that it is the tip-associated vortices around the free end that cause ECIV; i.e. the interpretation of the vibration is different from the idea of subharmonic oscillation.

The low-frequency Karman vortices, which were observed as a few tiny peaks in Figure 14(a), became dominant by increasing D_{cd}/D_c [Figure 14(b,c)], although the strength of the tip-associated vortices diminished. Figure 15 shows the span-wise distribution of the vortex shedding frequencies at several wind speeds in the case of attaching the disk of $D_{cd}/D_c = 2{\cdot}0$. In this case, the tip-associated vortices are not generated. The low-frequency Karman vortices, whose frequency is somewhat lower than the Karman vortex-shedding frequency, is found to be generated only around the free end. Also, comparing with Figure 8,

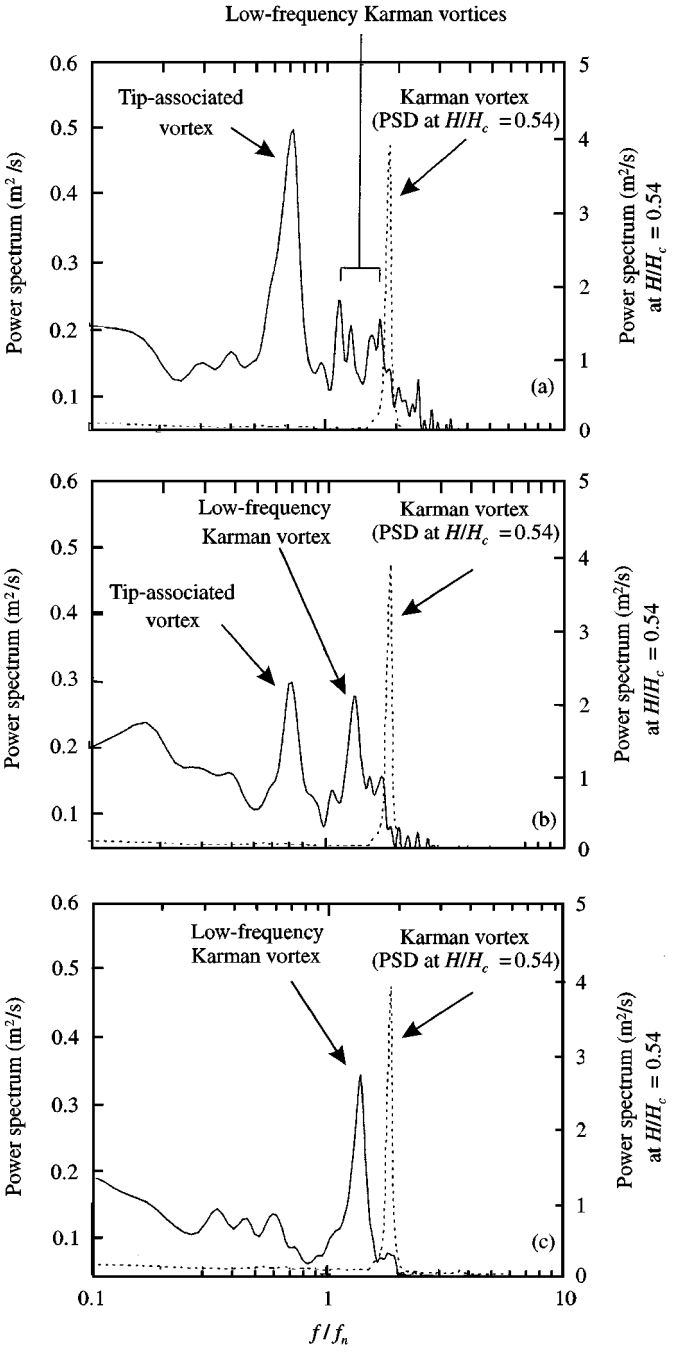

Figure 14. Power spectra of the wind velocity fluctuations behind the model at $H/H_c = 0{\cdot}92$ and $V/f_nD_c = 10$ in the case of (a) no disk, (b) $D_{cd}/D_c = 1{\cdot}2$, and (c) $D_{cd}/D_c = 1{\cdot}6$. For comparison, the power spectra at $H/H_c = 0{\cdot}54$ is illustrated with a dotted line.

we can see that the height where that vortex appears is nearly the same as the position where the tip-associated vortices are observed.

The relationship between the frequencies of vortices observed at $H/H_c = 0{\cdot}92$ and D_{cd}/D_c is summarized in Figure 16. The frequencies of vortex shedding are expressed as St, which

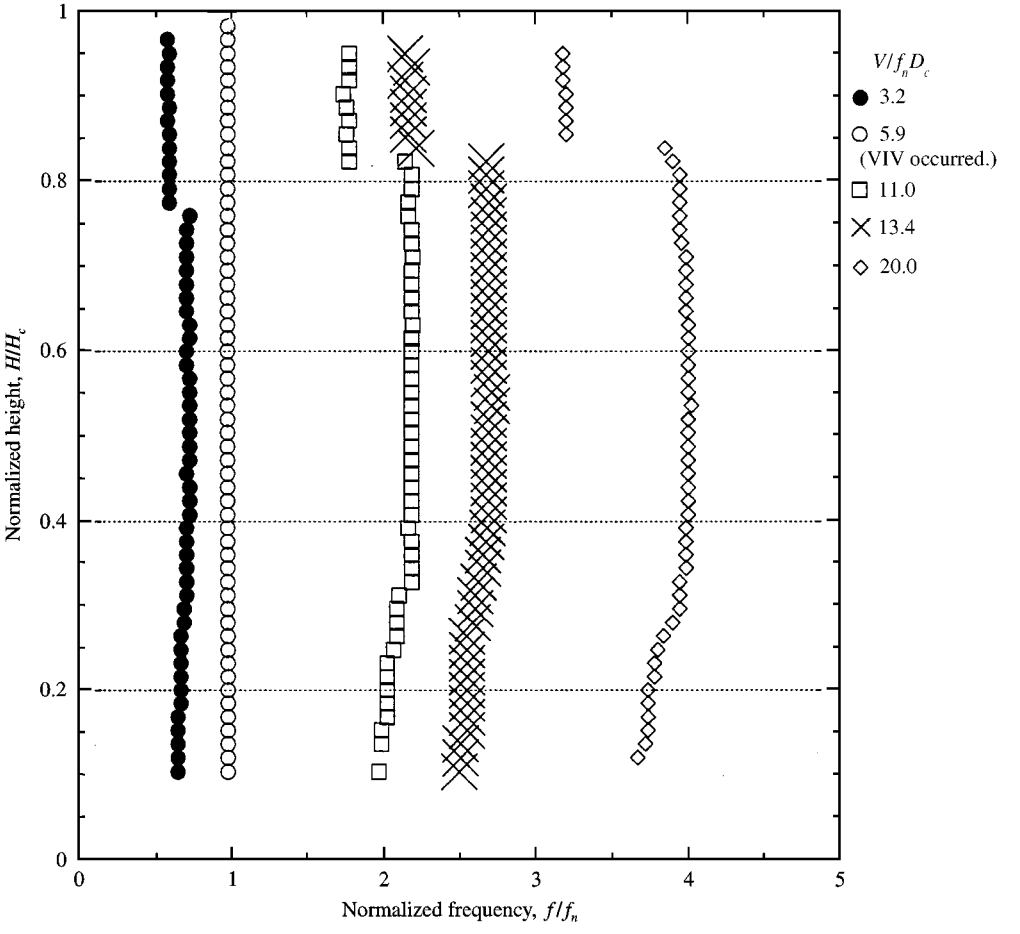

Figure 15. Span-wise distribution of vortex shedding frequencies at $V/f_nD_c = 3{\cdot}2$, 5·9, 11·0, 13·4 and 20·0 with a circular disk of $D_{cd}/D_c = 2{\cdot}0$ attached.

had no Reynolds number dependency within the present wind speed range. Additionally, for comparison, the values of St of the Karman vortex shedding at $H/H_c = 0{\cdot}54$ are also shown. When no disk was used ($D_{cd}/D_c = 1{\cdot}0$), the tip-associated vortex shedding with St = 0·07 was dominant at $H/H_c = 0{\cdot}92$, as shown in Figure 14(a). It is observed that St for the tip-associated vortices gradually increases with increasing D_{cd}/D_c. This is the reason why the response peak of ECIV moved to the low wind speed region as seen in Figure 13. Also, St for the low-frequency Karman vortices increased with increasing D_{cd}/D_c.

A question posed from the generation of the low-frequency Karman vortices is the possibility that it causes other vibration, since its frequency is different from the Karman vortex-shedding frequency. The frequency of the low-frequency Karman vortices for V/f_nD_c in the case of no disk is shown in Figure 17. Since, as shown in Figure 14(a), the generation of these vortices is very weak, the peak due to low-frequency Karman vortices cannot be determined uniquely. All frequencies thought to be due to these vortices are plotted. For comparison, the response amplitude is illustrated with a dotted line and the Karman vortex shedding frequencies at $H/H_c = 0{\cdot}54$ are plotted with blank dots. The frequency of the low-frequency Karman vortices was nearly proportional to V/f_nD_c in spite of dispersion. In the case of attaching the disk of $D_{cd}/D_c = 1{\cdot}6$ (Figure 18), it is apparent that the frequency of

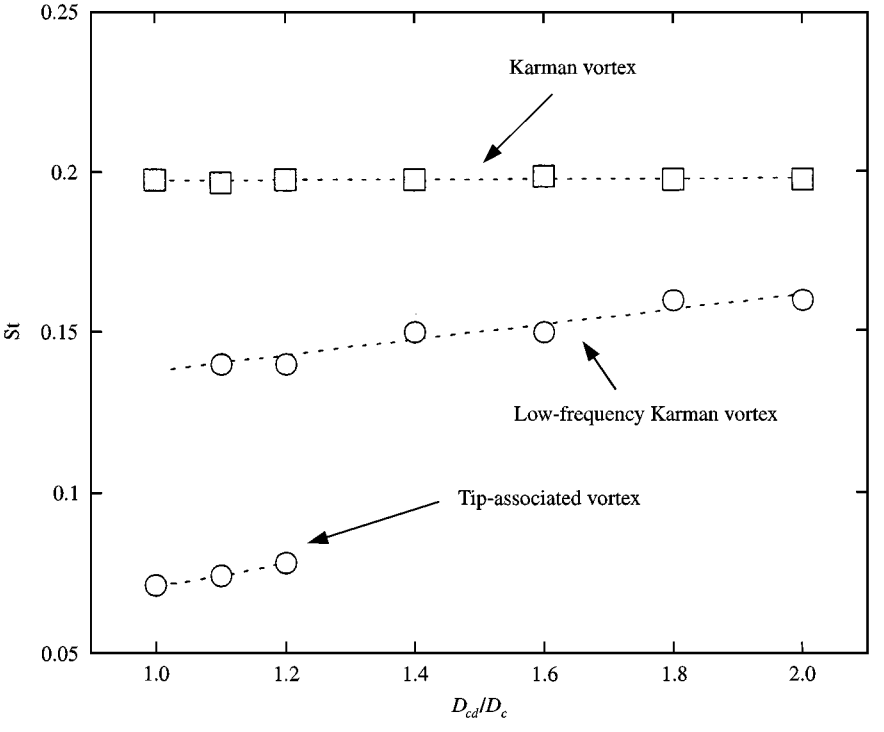

Figure 16. Effect of D_{cd} on vortex-shedding frequency at $H/H_c = 0{\cdot}92$ expressed as Strouhal number, St: □, $H/H_c = 0{\cdot}52$; ○, $H/H_c = 0{\cdot}92$. The Karman vortex-shedding frequency at $H/H_c = 0{\cdot}54$ was not influenced by D_{cd}.

the low-frequency Karman vortices is proportional to $V/f_n D_c$. In both Figures 17 and 18, its frequency locked-in to f_n around the wind speed range where VIV occurred and never coincides with f_n at other wind speeds. Hence the low-frequency Karman vortex shedding does not induce another response peak like ECIV.

Comparing Figure 17 with Figure 18, the lock-in wind speed range of the low-frequency Karman vortex shedding in the no-disk case is wider than that in the case of $D_{cd}/D_c = 1{\cdot}6$. Moreover, we can find that the wind speed range where VIV occurred in the case of no disk is larger than that in the case of a disk with $D_{cd}/D_c = 1{\cdot}6$, although the lock-in range of Karman vortices at $H/H_c = 0{\cdot}54$ is nearly the same in these two cases. This change of the occurrence range of VIV can be also observed in Figure 13. The lock-in region of the low-frequency Karman vortex with D_{cd}/D_c variation is summarized in Figure 19. The lock-in range gradually becomes smaller with increasing D_{cd}/D_c. This can be explained by the trend of St of the low-frequency Karman vortex shedding shown in Figure 16; i.e. St of the low-frequency Karman vortices increases with increasing D_{cd}/D_c, approaching value of the St for the regular Karman vortex shedding. It is thought that this change of lock-in range influences to the change of the threshold wind-speed range of VIV.

Some experimental studies [e.g., Gerich & Eckelmann (1982) and Williamson (1989)] showed that, even in the case of a two-dimensional circular cylinder with large end-plates, vortex shedding with a frequency lower than the regular shedding frequency around center of the span existed near the end-plate. There is a possibility that the low-frequency Karman vortex shedding here corresponds to that reported in those studies. However, Gerich & Eckelmann investigated the Strouhal number of that vortex in the rage of $\mathrm{Re} < 160$ and indicated that the St gradually became smaller as the end-plate diameter was increased. On

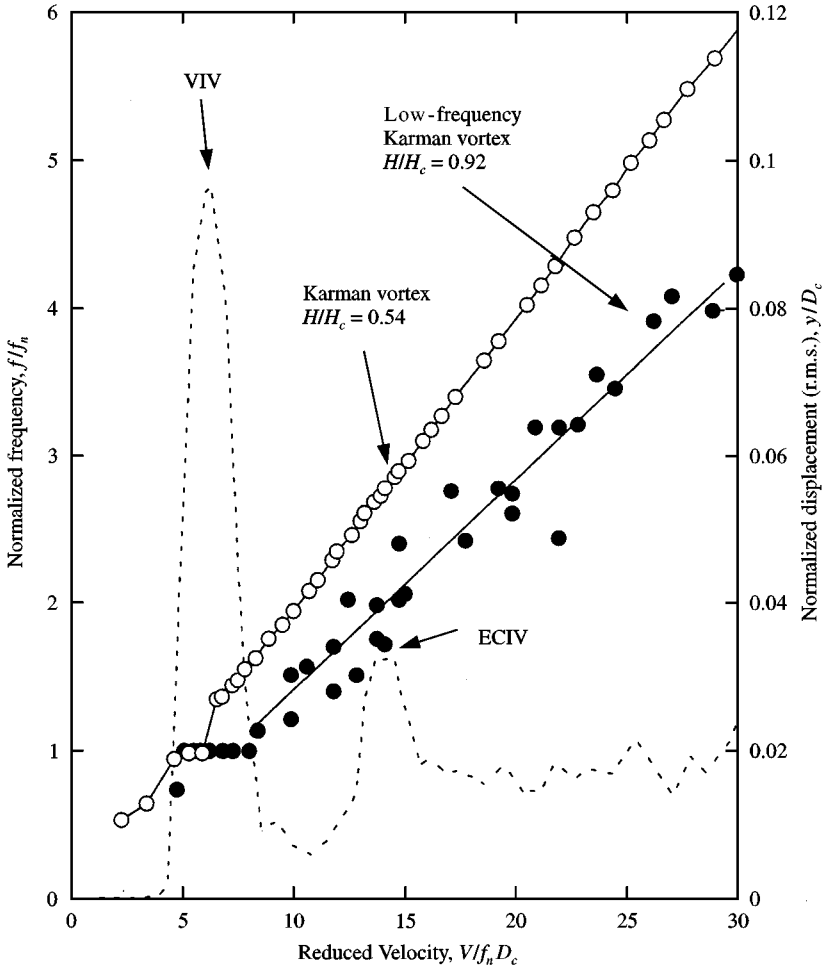

Figure 17. Relationship between vortex shedding frequencies and transverse-to-wind response of the model in the case of no disk attached.

the contrary, as shown in Figure 16, St for the low-frequency Karman vortex in the present experiment becomes larger with increasing D_{cd}. This is in contradiction to their results, although the range of Re in the present case is much higher than that in their experiments, and the present experimental model is three dimensional.

4. CONCLUSIONS

Wind tunnel experiments using a cantilever circular cylinder were carried out to investigate the characteristics of end-cell induced vibration (ECIV). The transverse-to-wind displacement of the model had not only the response peak due to VIV, but also that due to ECIV at a wind speed approximately three times higher than the threshold wind speed of vortex-induced vibration (VIV). The amplitude of ECIV was rather unsteady, while VIV was nearly steady as generally seen in VIV of low damping structures. The measurement of wind velocity fluctuations behind the model clarified that the tip-associated vortices appeared in the wake around the free end, and that its frequency was lower than the Karman vortex shedding frequency and nearly proportional to the wind speed. Since the response peak due

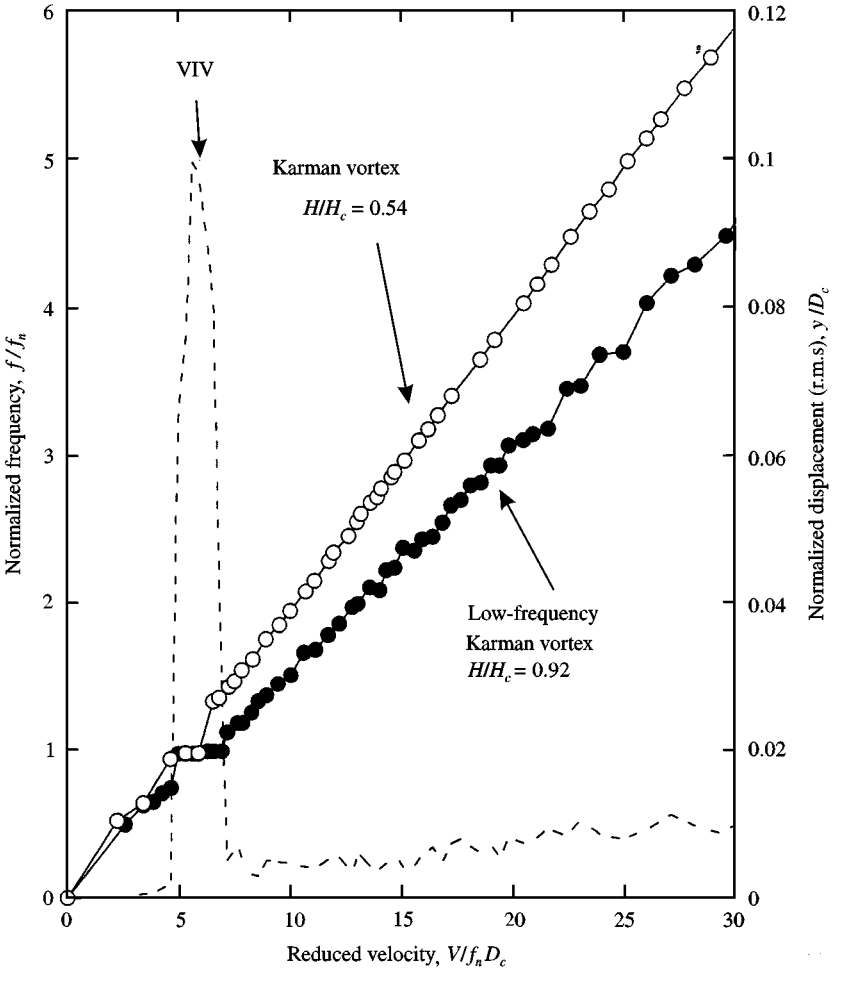

Figure 18. Relationship between vortex-shedding frequencies and transverse-to-wind response of the model in the case of $D_{cd}/D_c = 1{\cdot}6$.

to ECIV was observed at a wind speed where the frequency of the tip-associated vortices coincided with the natural frequency, it was considered that the ECIV was induced by the tip-associated vortices. This consideration was consistent with the result obtained by Kitagawa *et al.* (1998).

On the other hand, the phase shift of the tip-associated vortices, which was obtained by the wind velocity fluctuation measurement using two I-probes located symmetrically to the flow direction, was not constant, whilst that of the Karman vortex street was almost π (radians) and independent on the wind-speed range in this study. Hence, it is possibile that the mechanism of ECIV is different from that of classical VIV.

In order to study the effects of the free-end condition on the occurrence of ECIV and the generation of the tip-associated vortices, a circular disk was placed on the model top and its diameter was varied. It was shown that the response due to ECIV decreased, and the threshold wind speed was rather reduced as the disk diameter increased, although the amplitude of VIV was not influenced by the disk. This phenomenon could be explained by the decrease of the power of the tip-associated vortices and the slight increase of their frequency as the disk diameter is increased

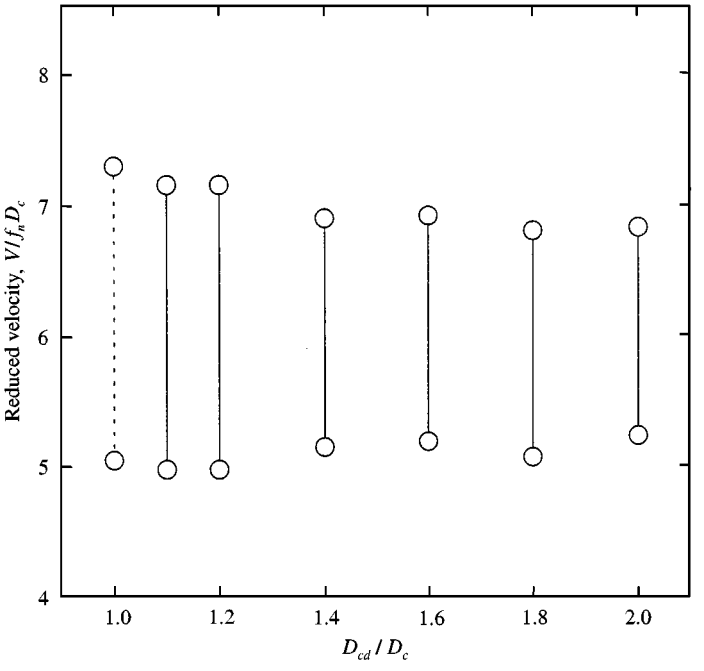

Figure 19. Relationship between the lock-in region of the low-frequency Karman vortex shedding and D_{cd}.

Also, when placing disks with diameter over 1·1 times larger than the model diameter, another vortex shedding was dominant around the model top while the tip-associated vortices disappeared. That was called low-frequency Karman vortex shedding in the present study. Its frequency was much higher than that of the tip-associated vortex shedding but somewhat lower than that of the regular Karman vortex shedding. The low-frequency Karman vortex shedding locked-in at the wind speed where VIV occurred and did not coincide with the natural frequency at a wind speed higher than that wind speed. Then, the low-frequency Karman vortices did not induce other response peaks like ECIV. Using the diffusive Van der Pol equation, Balasubramanian & Skop (1996) modeled the spanwise cellular structures of circular cylinders. It would be useful for simulating end effects on vortex shedding to apply their model to the present case.

In the present study, discussion was made on the relation of model response and wind velocity fluctuations in the wake. A point which we shall address in a future study is the investigation of the lift forces due to the tip-associated vortices. To do this, the measurement of surface pressures would be necessary, specifically paying more attention to the free-end portion. Furthermore, in wind tunnels it is difficult to visualize the detailed structure of the tip-associated vortices at high Reynolds number, because of complex turbulence in the wake near the free end. Visualization in water and some three-dimensional computational fluid–structure interaction simulations will be required.

ACKNOWLEDGEMENTS

The authors are grateful to Dr Toshihiro Wakahara and all research engineers of Fluid Dynamics Group in the Institute of Technology, Shimizu Corporation, for their continuous cooperation in the wind tunnel experiments, and Dr Takashi Nomura of Nihon University for his valuable comments on this study.

References

Ayoub, A. & Karamcheti, K. 1982 An experiment on the flow past a finite circular cylinder at high subcritical and supercritical Reynolds number. *Journal of Fluid Mechanics* **118,** 1–26.

Balasubramanian, S. & Skop, R. A. 1996 A nonlinear oscillator model for vortex shedding from cylinders and cones in uniform and shear flows. *Journal of Fluids and Structures* **10,** 197–214.

Durgin, W. W., March, P. A. & Lefebvre, P. J. 1980 Lower mode response of circular cylinder in cross-flow. *Transaction of ASME Journal of Fluids Engineering* **102,** 183–190.

Farivar, DJ. 1981 Turbulent uniform flow around cylinders of finite length. *AIAA Journal* **19,** 275–281.

Fox, T. & Apelt, C. J. 1993 Fluid-induced loading of cantilevered circular cylinders in a low-turbulence uniform flow. Part 3: Fluctuating loads with aspect ratios 4 to 25. *Journal of Fluids and Structures* **7,** 375–386.

Gerich, C & Eckelmann, H. 1982 Influence of end plates and free ends on the shedding frequency of circular cylinders. *Journal of Fluid Mechanics* **122,** 109–121.

Kawai, H. 1994 Vortex-induced vibration of tapered cylinder. *Journal of Wind Engineering* **59,** 49–52 (in Japanese).

Kawamura, T., Hiwada, M., Hibino, T., Mabuchi, I. & Kumada, M. 1984 Flow around the finite circular cylinder on a flat plate. *Bulletin of JSME* **27,** 2142–2151.

Khalak, A. & Williamson, C. H. K. 1996 Dynamics of a hydroelastic cylinder with very low mass and damping. *Journal of Fluids and Structures* **10,** 455–472.

Kitagawa, T., Wakahara, T., Fujino, Y. & Kimura, K. 1998 An experimental study on vortex-induced vibration of a circular cylinder tower at a high wind speed. *Journal of Wind Engineering and Industrial Aerodynamics* **69–71,** 731–744.

Okamoto, T. & Yagita, M. 1973 The experimental investigation on the flow past a circular cylinder of finite length placed normal to the plane surface in a uniform stream. *Bulletin of JSME* **16,** 805–814.

Ongoren, A. & Rockwell, D. 1988 Flow structure from an oscillating cylinder Part 1. Mechanisms of phase shift and recovery in the near wake. *Journal of Fluid Mechanics* **191,** 197–223.

Williamson, C. H. K. 1989 Oblique and parallel modes of vortex shedding in the wake of a circular cylinder at low Reynolds numbers. *Journal of Fluid Mechanics* **206,** 579–627.

Wootton, L. R. 1969 The oscillations of large circular stacks in wind. *Proceedings of Institution of Civil Engineers* **43,** 573–598.